Preparation, characterization, and far-infrared study of ceramic high-T_c superconductors

T. Zetterer, W. Ose, J. Schützmann, H. H. Otto, P. E. Obermayer, N. Tasler, H. Lengfellner, G. Lugert, J. Keller, and K. F. Renk

Fakultät für Physik, Universität Regensburg, 8400 Regensburg, Federal Republic of Germany

Received August 25, 1988; accepted November 16, 1988

We report on a study of single-phase (superconducting) $YBa_2Cu_3O_7$ and (nonconducting) Y_2BaCuO_5 and mixed phases of these compounds in bulk and film samples and on an investigation of ceramic bulk material of the homologous series $Tl_2Ba_2Ca_nCu_{n+1}O_{2n+6}$. We describe preparation and structural characterization by x-ray diffraction analyses and further characterization by electric, magnetic, tunnel junction, and Raman scattering studies, and we present results of far-infrared reflectivity measurements. In a theoretical analysis we relate the phonon structure of reflectivity spectra to geometric structure of a metallic network, with holes filled with nonconducting material. The influence of superconductivity on reflectivity is also investigated.

1. INTRODUCTION

The discovery of high-T_c superconductors of the $La_{2-x}Ba_xCuO_4$ (Ref. 1) and $YBa_2Cu_3O_{7-\delta}$ (Ref. 2) families and of the homologous series $Bi_2Sr_2Ca_nCu_{n+1}O_{2n+6-\epsilon}$ (Refs. 3–6) and $Tl_2Ba_2Ca_nCu_{n+1}O_{2n+6-\epsilon}$ (n = 0, 1, 2) (Ref. 7) has stimulated much activity in the investigation of cuprates.

We report on a far-infared reflectivity study of the ceramic high-T_c materials $YBa_2Cu_3O_7$ and $Tl_2Ba_2Ca_nCu_{n+1}O_{2n+6-\epsilon}$ (n = 0, 1, 2). In addition, we investigated (nonconducting) Y_2BaCuO_5 and phase mixtures. The far-infrared study was combined with a careful analysis by x-ray diffraction and with further characterization by a variety of other techniques.

There are various infrared studies of $YBa_2Cu_3O_7$ (Refs. 8–19) and a few studies of Y_2BaCuO_5 (Refs. 18, 20, and 21); a systematic far-infrared study of a *mixed-phase* sample was reported in Ref. 18. In the present study we show that in a phase mixture of conducting and nonconducting materials the phonon resonances of the nonconducting material have a strong influence on the far-infrared reflectivity. Correspondingly, in a single-phase polycrystalline material with different orientation of crystallites that have anisotropic dynamical conductivity, phonon resonances may be seen in large strength in the far-infrared reflection spectra; evidence is reported for the $Tl_2Ba_2Ca_nCu_{n+1}O_{2n+6-\epsilon}$ homologous series. We present a theoretical analysis that indicates that the phonon structure of the far-infrared reflectivity spectrum of a sample depends strongly on the geometric structure of the network of conducting material in the sample. The analysis permits extraction of characteristic parameters for the infrared-active phonon modes. Furthermore, information on the dynamic conductivity of materials in the normal and superconducting states is obtained.

2. SAMPLE PREPARATION AND CHARACTERIZATION

A. Preparation of $YBa_2Cu_3O_7$

We synthesized $YBa_2Cu_3O_{7-\delta}$ ($\delta \geq 0$) from appropriate amounts of Y_2O_3, $BaCO_3$, and CuO fine powders, usually mixed in a ball mill. The material was heated either as powder in Al_2O_3 crucibles or as pressed pellets in a furnace at a temperature of 950–970°C for a period of several hours. The samples usually contained, in addition to the $YBa_2Cu_3O_{7-\delta}$ phase, the so-called green phase Y_2BaCuO_5 and several other phases. To obtain single-phase (superconducting) $YBa_2Cu_3O_{7-\delta}$, we reground the samples, homogenized them well, pressed them into pellets (8 tons/cm^2), and fired them again at 950°C. Flowing oxygen was needed during the cooling period, and a longer stage (2 h) near 450°C was necessary for resorption of oxygen to form $YBa_2Cu_3O_{7-\delta}$ with $\delta \approx 0$. This resorption of oxygen leads to the transition from the tetragonal structure of $YBa_2Cu_3O_{6.5}$ (δ = 0.5) to the orthorhombic superconducting $YBa_2Cu_3O_{7-\delta}$ ($\delta \approx 0$).

We found that an additional annealing step resulted in an enhancement of far-infrared reflectivity of our samples. After the first heat treatment, the fine reground powder was annealed at 750°C for 10 h in flowing oxygen and cooled to room temperature within 2 h. One of the samples showed extraordinarily high far-infrared reflectivity (see Section 4 below), indicating high surface quality. This sample also showed a large Meissner effect. We do not know which special conditions were responsible for the difference from the other samples, which were prepared by almost the same procedure but had lower far-infrared reflectivity.

B. Characterization of $YBa_2Cu_3O_7$

Our samples were characterized by x-ray powder diffraction to determine the lattice constants as well as to find out the content of foreign phases in the samples. The x-ray powder diffraction pattern of $YBa_2Cu_3O_7$ is shown in Fig. 1(a). For the orthorhombic unit cell (space group *Pmmm*) we found the lattice constants a = 3.8194(8) Å, b = 3.8883(8) Å, and c = 11.6677(2) Å, which agree with published data.[22,23]

In Fig. 1(b) we show a Bragg–Brentano diagram of the surface of our highly reflecting sample. A comparison with Fig. 1(a) indicates that a texture with preferential c-axis orientation perpendicular to the sample surface occurred. For a further characterization of the sample, electron microscope pictures were taken. The pictures, published else-

0740-3224/89/030420-16$2.00

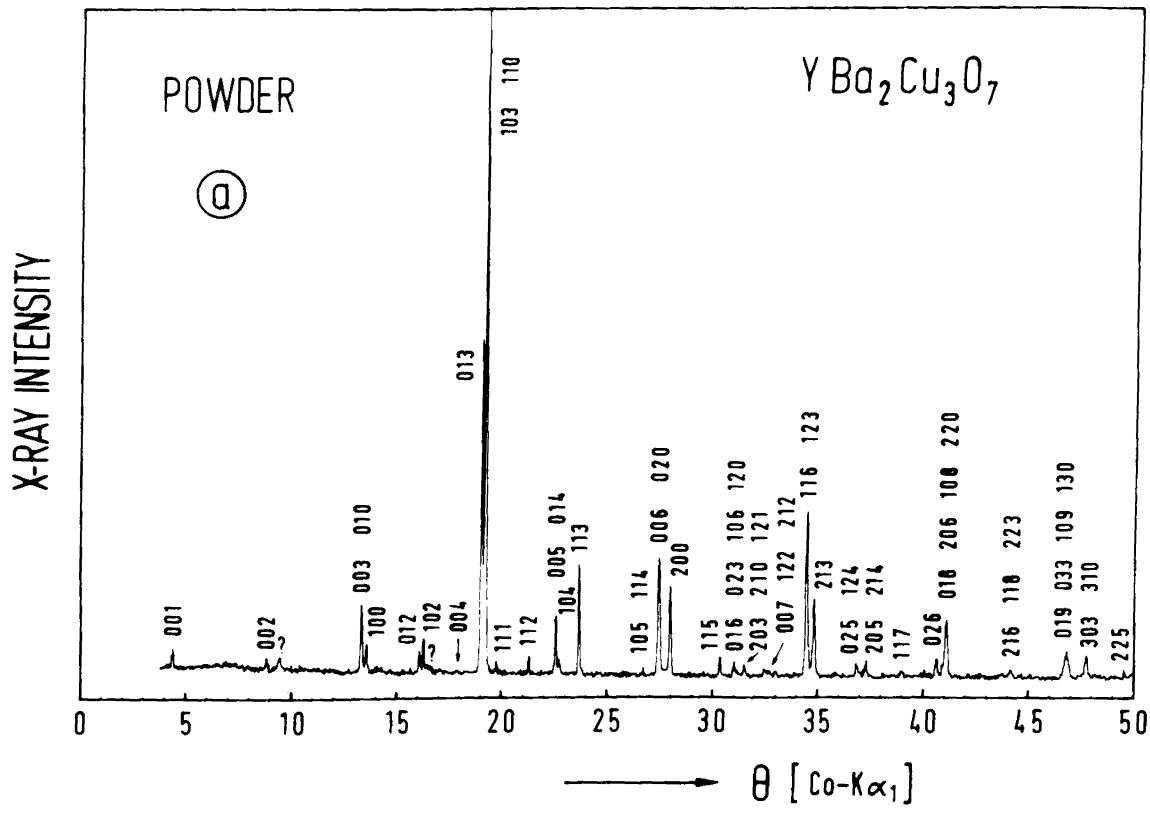

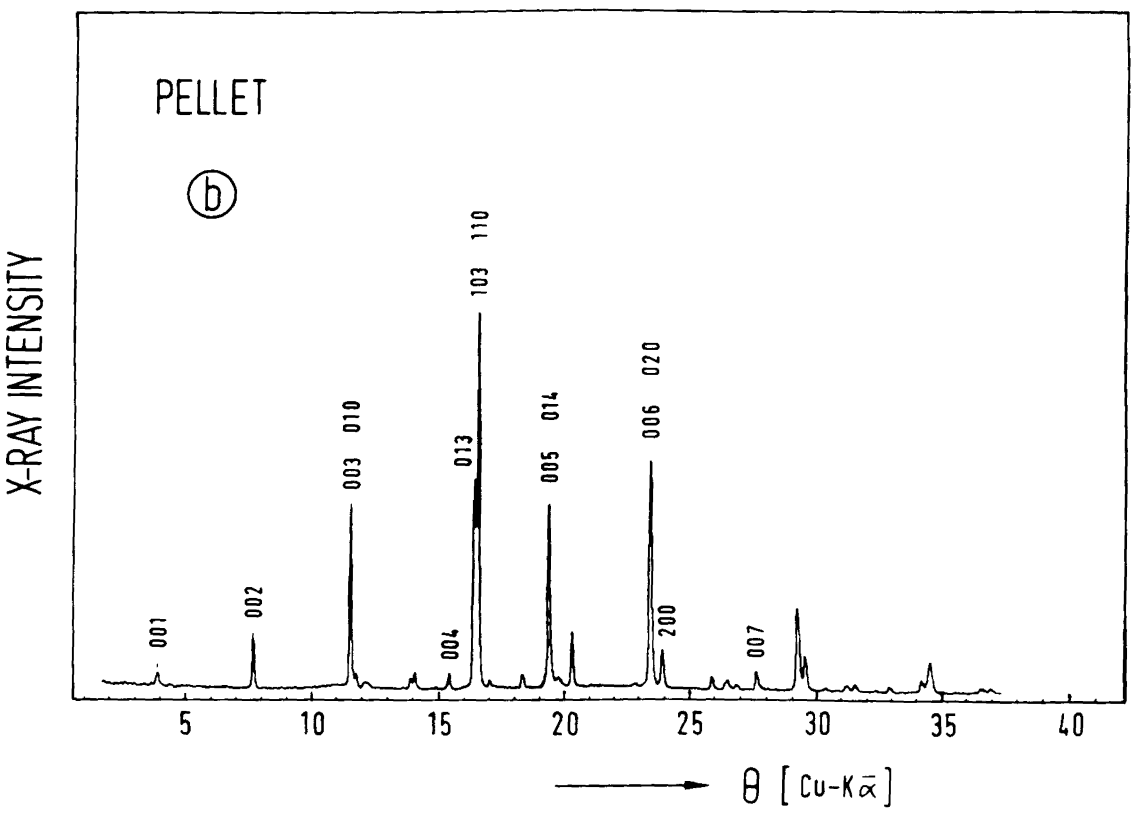

Fig. 1. X-ray diffraction pattern for $YBa_2Cu_3O_7$: (a) powder diagram, (b) Bragg–Brentano diagram.

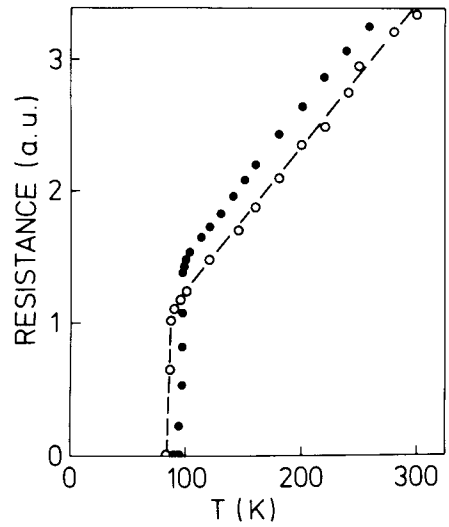

Fig. 2. Resistance of $YBa_2Cu_3O_7$ for our highly reflecting sample (open circles) and our sample with the highest T_c (filled circles).

where,[19] show that large areas of the sample are covered with platelets (typical size 2 μm × 8 μm) with the crystallographic c axis perpendicular to the surface, in agreement with the x-ray analysis.

The resistances, measured by the standard low-frequency four-probe method with silver-paint contacts, are shown in Fig. 2 for our $YBa_2Cu_3O_7$ sample with the highest value of T_c ($\simeq$94 K) and for the sample ($T_c \simeq$ 86 K) that showed highest far-infrared reflectivity. The resistances decrease linearly with decreasing temperature, and the transitions to superconductivity are sharp ($\Delta T_c \approx 2$ K). The specific resistances at room temperature were ~300 $\mu\Omega$ cm.

C. Point-Contact Tunnel Spectroscopy on $YBa_2Cu_3O_7$

Point-contact tunneling measurements initiated in various laboratories have been published. From these measurements superconducting energy gaps with values of $2\Delta/kT_c$ from approximately 3 to 6 were deduced.[24-27]

To obtain information on the existence of a superconducting energy gap, we also performed a tunneling experiment. Applying the four-terminal method, we measured the current–voltage (I–V) characteristic, using a point contact consisting of an electrolytically etched tungsten tip (diameter $\approx$1 μm) as one electrode and the surface of the $YBa_2Cu_3O_7$ sample as the other electrode. The tungsten tip was placed upon the $YBa_2Cu_3O_7$ sample by use of a differential screw. Contact resistivities from several kilohms to 1 MΩ were obtained. To prevent distortion or slipping off of the tungsten tip, the tungsten wire was bent into an elastic knee. The sample with the tip was immersed in liquid helium at a temperature of 4.2 K.

An I–V characteristic with evidence of a gap is shown in Fig. 3. At small voltages a vanishing current is obtained. The current increases strongly for $V \geq 10$ mV and behaves linearly for large voltages ($V \geq 30$ mV). From this measurement a lower limit for the gap of $\Delta \simeq 10$ meV ($2\Delta/kT_c \simeq 2.4$) may be deduced. For a further analysis we compare the theoretically expected characteristic

$$I = P_{12}N_1(0)N_2(0)\mathrm{Re}\{[(eV)^2 - \Delta^2]^{1/2}\} \qquad (1)$$

for $eV \geq \Delta$ and $I = 0$ for $eV < \Delta$, where P_{12} denotes the tunneling probability, $N_1(0)$ is the density of states at the Fermi level of the normal metal, is $N_2(0)$ the density of states at the Fermi level of $YBa_2Cu_3O_7$ (neglecting superconductivity), and the last term takes into account the superconducting state.

The dotted curve of Fig. 3 shows the theoretical characteristic for $2\Delta/kT_c = 4.6$. A better agreement with the experiment is obtained by choosing two, instead of one, different energy-gap values (with $2\Delta/kT_c = 3.3, 7$) and adding the corresponding currents. The resulting I–V characteristic (solid curve of Fig. 3) describes the experimental data well. Two different energy gaps (or a distribution of gaps) may be caused by crystallites of different orientations. A further discussion is given below in connection with far-infrared studies (Section 5).

D. Ac Josephson Effect in $YBa_2Cu_3O_7$ Break Junctions

To obtain information on the superconducting charge carriers in $YBa_2Cu_3O_7$, we studied the influence of microwave radiation on Josephson junctions. For preparation of clean Josephson junctions a break-junction technique[28] was applied. A $YBa_2Cu_3O_7$ sample was broken mechanically in liquid helium (at 4.2 K), and microwave radiation (power $\approx$1 mW) at a frequency $\nu_r = 9.52$ GHz was irradiated into the cryostat that contained the junction. Steps in the I–V characteristic are expected at voltages V_n at which the nth harmonic of the frequency of the microwave radiation corresponds to the Josephson frequency ν_f:

$$\nu_f = qV_n/h = \pm n\nu_r, \qquad (2)$$

where q denotes the charge of the superconducting charge carriers. The shape of the I–V characteristic depended strongly on microwave intensity. Characteristic curves that show the steps well are drawn in Fig. 4. The structure corresponds to steps at voltages (with $V_{n+1} - V_n \simeq 19.7$ μV) for q that are twice the elementary charge. The height of the single steps may be related to the microwave intensity by Bessel functions of the first kind. Half-integer multiples

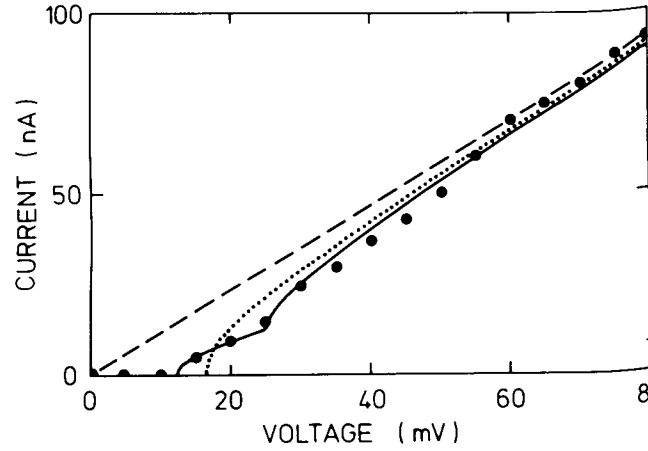

Fig. 3. Current-voltage characteristic of a tungsten tip on $YBa_2Cu_3O_7$: experiment (filled circles); theory with one gap (dotted curve) and two gaps (solid curve). The dashed line represents the linear I–V characteristic, typical, i.e., for a normal metal without any energy gap.

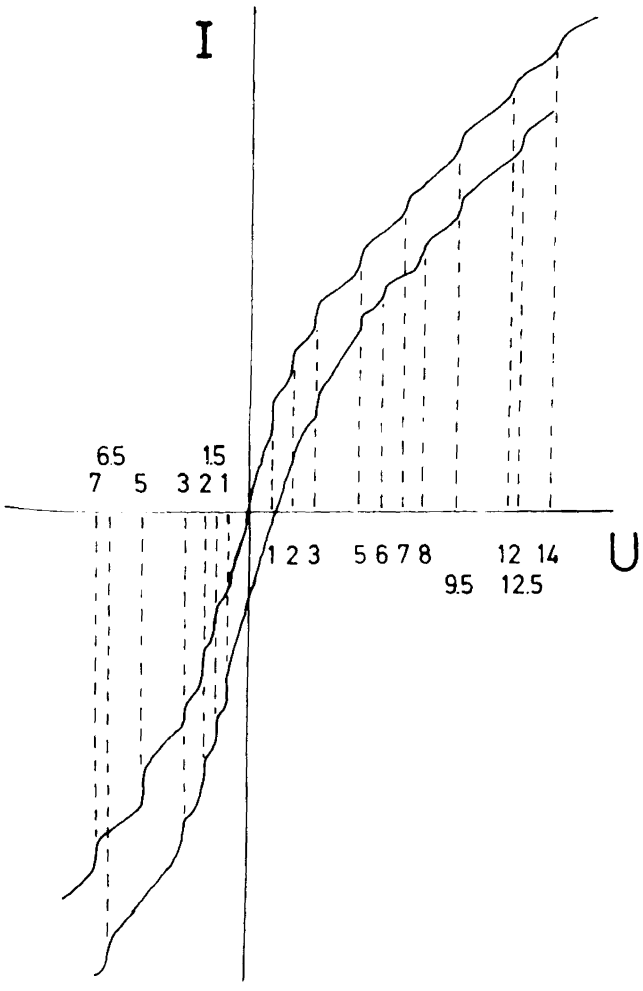

Fig. 4. Current-voltage characteristic of $YBa_2Cu_3O_7$ Josephson break junction under microwave irradiation (with the lower curve shifted); numbers, *n*th harmonics of the microwave frequency (9.5 GHz) corresponding to Josephson frequencies.

were also observed (Fig. 4). This suggests the additional existence of point-contact Josephson junctions because point contacts generally show steps at subharmonics of the microwave frequency. Thus we have demonstrated that our samples show characteristic superconducting properties. We note that our results agree with published results obtained by use of break junctions[28] and film break junctions[29] and also of point contacts[30] and microbridgelike junctions.[31]

E. Characterization of (Nonconducting) Y_2BaCuO_5

An x-ray powder diffraction pattern is shown in Fig. 5; only for the main peaks have we indicated the corresponding indices. From an analysis of the pattern we found, for the orthorhombic unit cell (space group *Pbnm*), the lattice constants a = 7.132 Å, b = 12.181 Å, and c = 5.658 Å for the insulating Y_2BaCuO_5. The values are the same as those in Ref. 22.

F. Preparation of Single-Phase, Polycrystalline $Tl_2Ba_2Ca_nCu_{n+1}O_{2n+6}$ (n = 0, 1, 2)

The n = 0, 1, 2 members of the homologous series $Tl_2Ba_2Ca_n$-$Cu_{n+1}O_{2n+6-\epsilon}$, denoted the 2201, 2212, and 2223 phases, respectively, were prepared by mixing appropriate amounts of Tl_2O_3, $Ba(NO_3)_2$, CaO, and CuO. Pressed pellets, usually 13 mm in diameter and 10 mm thick, were placed, together with a gold boat containing a small amount of Tl_2O_3, into an aluminum oxide crucible covered with a tight lid. Under these conditions there was a saturated Tl_2O vapor during the annealing procedure; thus Tl loss due to the high volatility of thallium oxides was minimized or avoided. The samples were heated at a rate of 200°C/h up to 800°C and held at this temperature for 8 h, cooled down to 600°C within 2 h, and then taken out of the furnace.[32] The sintered material was reground and pressed again into pellets (10 tons/cm^2) 2–3 mm thick.

The second heat treatment was different for the three phases. The superconducting, tetragonal 2201 (t-2201) phase was obtained if pellets with the appropriate stoichiometry were fired at 850°C in air for half an hour and then quenched to liquid-nitrogen temperature. Annealing in flowing oxygen at 800°C and cooling in the furnace to room temperature lead to the orthorhombic (normally conducting) 2201 (o-2201) phase.

The (superconducting) 2212 phase was obtained by annealing a sample of adequate stoichiometry at 820°C in flowing oxygen for 30 min, furnace cooling to 600°C, and quenching to room temperature after 1 h. Even if the stoichiometry of the original mixed powders has been 2223, the 2212 phase was formed under these conditions, and a calcium-rich Ca–Tl–Cu–O (CaTlCu) phase with previously unknown structure, and several other phases, were also found. A detailed analysis of the CaTlCu phase is in progress. As a result of far-infrared reflection measurements, it was essential to have the same phase at the surface as in the bulk material. Therefore during the second annealing procedure we placed the pellets into a closed bag (formed by a gold foil) that also contained some Tl_2O_3. Then we obtained samples with a well-conducting surface and with the same composition as the bulk material. Thus contact problems with dc conductivity measurements were also avoided.

The 2223 phase, with the highest T_c, was obtained by annealing a 2223 sample in air at 840°C for 5 min, furnace cooling to 600°C, holding it 90 min, and then quenching it to room temperature. Now only the surface region of the pellets contained CuO, CaTlCu, and an unidentified phase. After the material of the surface region was removed, the x-ray powder diffraction diagram [Fig. 6(d)] of the bulk material showed almost single-phase $Tl_2Ba_2Ca_2Cu_3O_{10}$, with an admixture of a small amount of the 2212 phase (arrows).

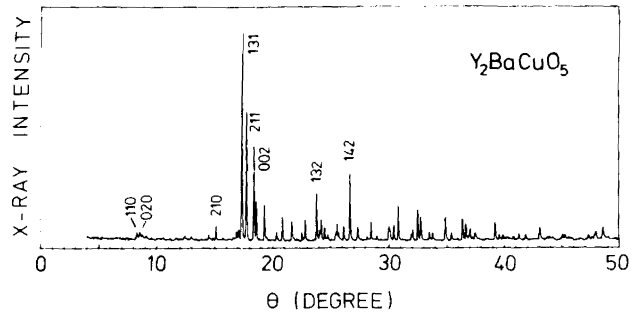

Fig. 5. X-ray powder diagram for Y_2BaCuO_5.

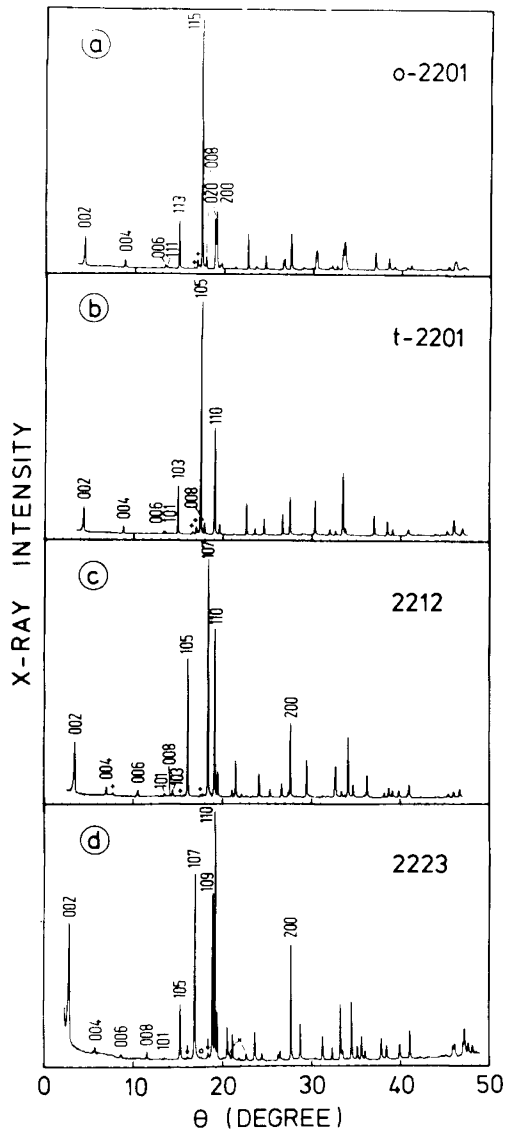

Fig. 6. X-ray powder diagrams for the homologous series $Tl_2Ba_2Ca_nCu_{n+1}O_{2n+6}$ (n = 0, 1, 2).

We did not succeed in preparing a 2223 sample with highly conducting surfaces, i.e., without foreign phases in the surface area.

G. Characterization of $Tl_2Ba_2Ca_nCu_{n+1}O_{2n+6}$

We performed complete structure analyses for the two 2201 phases and the 2212 and 2223 phases.[33] The x-ray diffraction diagrams for the different phases (Fig. 6) indicate that only small amounts (<3%) of foreign phases were contained in the samples.

The most striking feature of the diffraction patterns is the stepwise shift of the (002) diffraction peak toward smaller angles with increasing n, indicating an increase of the lattice constant in c direction. A short summary of our results is given in Table 1; for further crystallographic data see Refs. 34 and 35. Dc conductivity measurements were performed for the different phases. All samples showed metalliclike behavior (Figs. 7 and 8). The transition temperatures increased with increasing n. Additional data are given in Table 2; T_c denotes zero resistance temperature, T_{cm} the temperature of the transition midpoint, and ΔT_c the difference between $T_{90\%}$ and $T_{10\%}$.

For the 2201 phase, T_c is strongly dependent on the second annealing process. We believe that T_c is maximized by fast quenching from the highest temperature at which the 2201 phase is stable. A disadvantage of this procedure is the destruction of the smooth surface at temperatures higher than 860°C.

We note that it is possible to describe the conductivity of the 2221 phase (Fig. 8) by the expression $\sigma(T) = (\rho_0 + \alpha T)^{-1} + \Delta\sigma$, where $\rho_0 \simeq 50\ \mu\Omega$cm, $a \simeq 1\ \mu\Omega$cm K^{-1}, and $\Delta\sigma$ is an additional conductivity that describes the deviation of the $\rho(T)$ curve from a linear curve. We find that the additional conductivity can be described by two-dimensional superconducting fluctuations,[36] $\Delta\sigma = e^2(16\hbar\eta)^{-1}T_c(T - T_c)^{-1}$, with η ($\simeq$3 Å) being a characteristic thickness of the two-dimensional system; a calculated curve agrees well (within 1% accuracy) with the experimental curve. A definition by three-dimensional fluctuations, with $\Delta\sigma = e^2[32\hbar\xi(0)]^{-1}T_c^{1/2}(T - T_c)^{-1/2}$, does not deliver a reasonable description, because then we find an unrealistic coherence length $\xi(0) \simeq 0.4$ Å.

Using a SQUID magnetometer, we carried out static magnetic susceptibility measurements. Bulk samples (with typical dimensions of 2 mm × 2 mm × 2 mm) were cut from pellets, and magnetic shielding and the Meissner effect were measured in a procedure[37] illustrated in Fig. 9; first the samples were cooled in zero magnetic field down to ~5 K. After a magnetic field (3 mT) was applied, a diamagnetic magnetization appeared as a result of superconducting shielding currents. The experimental curves (Fig. 9) show some interesting features. When the samples are heated the shielding signal shows a step for the 2212 and 2223 phases but not for the t-2201 phase. This step can be explained by the deletion of shielding currents through Josephson junctions, as was pointed out in Ref. 38. For the t-2201 phase we obtained the high value of ~93% Meissner signal in comparison with the low-temperature shielding signal, whereas 17%

Table 1. Crystallographic Data for $Tl_2Ba_2Ca_nCu_{n+1}O_{2n+6}$ Phases

	Phase			
	o-2201	t-2201	2212	2223
Space group	*Amaa* or *A2aa*	*I4/mmm*	*I4/mmm*	*I4/mmm*
a (Å)	5.4474 (5)	3.8656 (3)	3.8565 (4)	3.8496 (4)
b (Å)	5.4948 (5)			
c (Å)	23.1795 (17)	23.2247 (18)	29.326 (3)	35.638 (4)
Cell volume (Å^3)	693.817	347.043	426.154	528.134
Formula units per cell	4	2	2	2

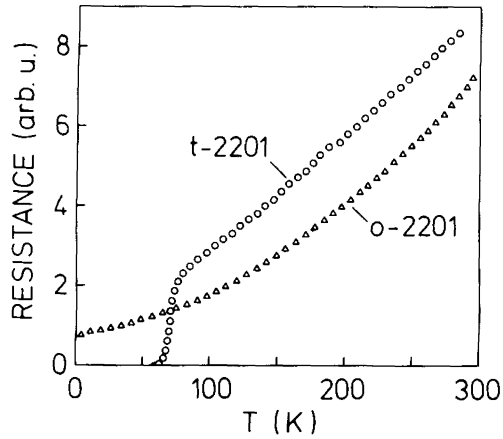

Fig. 7. Resistance of $Tl_2Ba_2CuO_6$ in the orthorhomic (o) phase and in the tetragonal (t) phase ($T_c \simeq 54$ K).

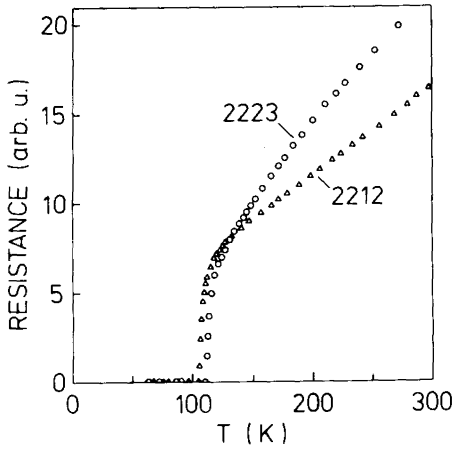

Fig. 8. Resistance of $Tl_2Ba_2CaCu_2O_8$ ($T_c \simeq 105.5$ K) and $Tl_2Ba_2Ca_2Cu_3O_{10}$ ($T_c \simeq 110.4$ K).

Table 2. Characteristic Temperatures for $Tl_2Ba_2Ca_nCu_{n+1}O_{2n+6}$ Compounds

Phase	T_c (K)	$T_{c,onset}$ (K)	T_{cm} (K)	ΔT_c (K)
2201	64	72	70	4
2212	105.5	110	107	2
2223	110.4	115	113	3

for the 2212 phase and 32% for the 2223 phase were found. This indicates that the t-2201 phase sample was highly homogeneous and that shielding currents flow nearly unrestrained between different grains. However, the relatively large transition width of the electrical resistance together with the (not particularly steep) slope of the magnetization curve points to the existence of different grains with different T_c values. This may be due to spatial variation of the oxygen or thallium portions of the sample caused by the final heat treatment in air. Similarly, the Meissner signal of the 2223 phase [Fig. 9(c)] appears to indicate a multiphase nature of the sample, too. In addition to a broad transition, coinciding with the transition of the electrical resistance, a step near 65 K was observed, with an enhancement of the diamagnetic signal by 20%. The reason for this enhancement is not yet clear. We note that the 2212 phase sample [Fig. 9(b)] and the 2223 sample [Fig. 9(c)] were identical with samples used for far-infrared studies.

H. Raman Study of the $Tl_2Ba_2Ca_nCu_{n+1}O_{2n+6}$ (n = 0, 1, 2) Series

For excitation of Raman emission we used an argon-ion laser (power 100 mW) operating at 488.0 or 514.5 nm; plasma lines were suppressed with a prism monochromator as the filter. The light was focused with a cylindrical lens onto a spot of approximately 0.5 × 4 mm on the sample. Raman-scattered light was analyzed by use of a double-grating monochromator, a photomultiplier, and standard pulse-counting techniques. The spectral bandpass was 5 cm^{-1}, and the signal integration time per inverse centimeter was ~30 sec. For a first survey we performed experiments with samples from bulk-fracture surfaces and from untreated surfaces at room temperature. Figure 10 shows Raman spectra for the four phases. Common to all phases are two resonances, near 490 and 600 cm^{-1}.

The 2212 phase shows another strong resonance near 530 cm^{-1}; this peak is most likely also present in the 2223 phase. A weak resonance at 640 cm^{-1} for the 2223 phase is probably due to nonreacted CuO.[39] There are further weaker resonances in the Raman spectra of all phases at smaller frequencies, which we did not study further.

We suggest that the two prominent peaks common to all phases (Fig. 10) can be attributed to Cu–O vibrations. The additional strong mode for the 2212 phase may be correlated with the calcium plane. Instead of oxygen octahedra in the 2201 phase, the oxygen atoms have a pyramidal arrangement in the 2212 phase. Therefore additional Raman-active pho-

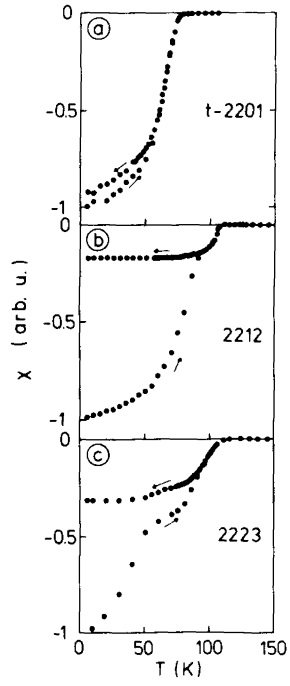

Fig. 9. Dc susceptibility of the superconducting $Tl_2Ba_2Ca_nCu_{n+1}O_{2n+6}$ (n = 0, 1, 2) phases at an applied field of 3 mT; Meissner signals and shielding signals after zero field cooling; data normalized to the low-temperature shielding signals.

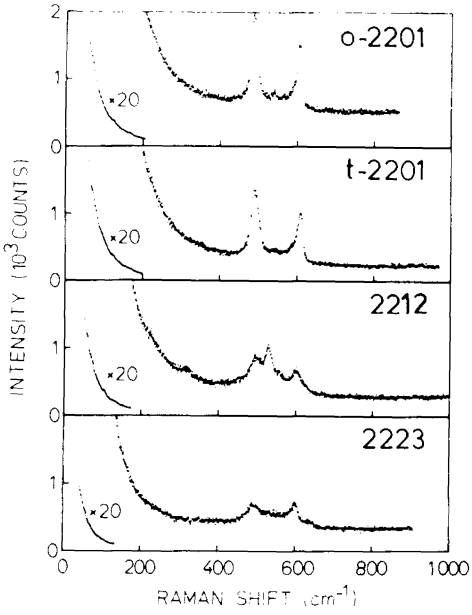

Fig. 10. Raman signals for the $Tl_2Ba_2Ca_nCu_{n+1}O_{2n+6}$ (n = 0, 1, 2) phases.

non modes can occur. A comparison with $YBa_2Cu_3O_7$ Raman spectra[40] shows that the strong resonances in the thallium compounds appear at noticeably larger frequencies; the largest, strongly Raman-active mode for $YBa_2Cu_3O_7$ is found near 500 cm^{-1}. As a result, the Raman spectra show that the phonon density of states extends in the thallium compounds at least up to a frequency of 600 cm^{-1}. A further discussion of the phonon modes is given in Subsection 5.B below.

3. TECHNIQUE OF FAR-INFRARED REFLECTIVITY MEASUREMENT AND METHODS OF ANALYSIS

A. Technique of Far-Infrared Reflectivity Measurement

Our reflectivity measurements were performed with an infrared Fourier spectrometer (Bruker IFS 113V). We used a variety of beam splitters and different detectors, namely, a liquid-helium-cooled silicon bolometer for small frequencies (20 to 650 cm^{-1}) and a liquid-nitrogen-cooled mercury–cadmium telluride detector for larger frequencies. Radiation within a solid angle of $\sim(1/8)\pi$ at an average angle of incidence (and reflection) of $\sim 10°$ was focused to a spot on the sample a few millimeters in diameter; the sample was placed in a cryostat. Besides specular reflectivity we also measured the sum of both specular and diffuse reflectivity. Then, radiation within a solid angle of almost π was focused onto the sample under an average angle of incidence of 45° by an elliptical mirror (at room temperature). Radiation reflected diffusively within a solid angle of π, together with the radiation reflected specularly under an average angle of reflection of 45°, was collected with a second elliptical mirror. Thus a large portion of diffusely reflected radiation was detected together with the specularly reflected radiation.

The temperature-variable cryostat had an inner chamber in which the sample was cooled by helium-exchange gas. Thus it was possible to regulate the sample temperature in a well-defined way. Optical access was through two windows; one closed the inner chamber tightly against a vacuum chamber, and one closed the vacuum chamber against air. The far-infrared radiation had to cross the two windows twice. As window materials we chose polyethylene at small frequencies and ZnSe and KBr at large frequencies. We used a mechanical arrangement that permitted an exchange of the sample, at fixed temperature, against a plane mirror and measurement of the spectral intensity with the sample as the reflector and with the mirror as the reflector; from the ratio of the reflected intensities, the reflectivity of the sample was determined. As the reference mirror we used either a gold-coated glass mirror or a bulk-molybdenum mirror. A comparison showed that the reflectivities of the two mirrors were equal within an error of less than 1% (measured between 20 and 600 cm^{-1}). For determination of the sample reflectivity a correction was made by calculating the mirror reflectivities from dc conductivities of the mirror materials; the correction was smaller than 1% (at frequencies up to 600 cm^{-1}). Using a sample–mirror exchange arrangement, we were able to eliminate the structure seen in the spectral intensities that was due to interferences and absorption peaks in the polyethylene windows. Additionally, we chose a polyethylene modification that was relatively weakly absorbing in the range of 400 to 700 cm^{-1}. The polyethylene windows had a thickness of $\sim$1 mm. Our sample–mirror arrangement showed good reproducibility for reflectivity values at various temperatures. We estimate that the absolute reflectivity values were accurate within few percent. This accuracy is sufficient for a first survey; it needs, however, to be increased. We did not polish the sample surfaces in order to avoid effects caused by polishing materials.

B. Methods of Analysis

For a first analysis we describe the ceramic material with a homogeneous medium theory, using the complex dynamic conductivity $\sigma = \sigma_1 + i\sigma_2$ that we decompose into a sum

$$\sigma = \sigma^p + \sigma^c + \sigma^b, \tag{3}$$

where $\sigma^p = \sigma_1^p + i\sigma_2^p$ is the contribution to the complex conductivity by phonons, $\sigma^c = \sigma_1^c + i\sigma_2^c$ is that by free charge carriers, and $\sigma^b = \sigma_1^b + i\sigma_2^b$ is that by bound charge carriers. The dynamic conductivity is connected to the dielectric function ϵ by the relation $\epsilon = i\sigma/\omega\epsilon_0 = i\sigma/(2\pi\nu c\epsilon_0)$, where ω is the angular frequency, ν is the frequency (divided by c), $\epsilon_0 = 8.9 \times 10^{-12}$ A-sec V^{-1} m^{-1}, and c is the velocity of light.

We describe the dynamic conductivity due to phonons by Lorentzian resonances

$$\sigma^p = -i(2\pi\nu c\epsilon_0) \sum_j S_j \nu_j^2 (\nu_j^2 - \nu^2 - i\Gamma_j \nu)^{-1}, \tag{4}$$

where S_j is the change of the dielectric function, $S_j\nu_j^2$ is the oscillator strength, ν_j is the eigenfrequency, and Γ_j is the damping constant for the jth phonon mode.

For the free-carrier conductivity we make use of Drude's conductivity

$$\sigma^c = \sigma_n(1 - i\nu/\nu_\tau)^{-1}, \tag{5}$$

where σ_n may be used here as a conductivity parameter that is not necessarily equal to the dc conductivity as for conventional metals and where ν_τ is the scattering rate of the free

carriers; from the relation $\sigma_n = 2\pi c\epsilon_0 \nu_p^2/\nu_\tau$ the plasma frequency ν_p can be obtained. At small frequencies, $\nu \ll \nu_\tau$, we have

$$\sigma^c \simeq \sigma_n + i\sigma_n \nu/\nu_\tau. \tag{6}$$

Neglecting the imaginary part, we obtain for the reflectivity the Hagen–Rubens approximation

$$R = 1 - (16\pi\epsilon_0 c\nu/\sigma_n)^{1/2}. \tag{7}$$

For the bound charge carriers we neglect the real part of the conductivity and write

$$\sigma^b = -i(2\pi\nu c\epsilon_0\epsilon_\infty), \tag{8}$$

where ϵ_∞ is the high-frequency dielectric constant.

We analyzed some of our reflectivity curves by using Kramers–Kronig analysis.[19] For this purpose we extrapolated the reflectivity curves at large frequencies ($\nu > 8000$ cm^{-1}) by Drude conductivity [Eq. (5)] and, taking into bound charges account, by Eq. (8). For an extrapolation of the reflectivity curves toward low frequencies we used Eq. (7), taking for σ_n a (constant) value that delivered a reasonable description of experimental reflectivity curves at small frequencies (20 to ~100 cm^{-1}).

For a discussion of the dynamic conductivity and the far-infrared reflectivity of superconductors we refer to the theory of Mattis and Bardeen[41,42] for BCS superconductors. Accordingly, σ_1 should be zero for $0 < \nu \leq \nu_g = 2\Delta/hc$, where 2Δ is the superconducting energy gap and ν_g is the corresponding gap frequency; σ_2 should show an approximately ν^{-1} dependence, with a value $\nu_2(\nu_g) \simeq \sigma_n$. It follows then that the reflectivity in the superconducting state is higher than in the normal state for $\nu \leq \nu_g$ and that it is lower for $\nu > \nu_g$; for the dirty limit a crossing point of the reflectivities at $\nu \simeq 2\nu_g$ is calculated.

4. FAR-INFRARED REFLECTIVITY

A. Reflectivity of $YBa_2Cu_3O_7$

Figure 11 shows the reflectivity of $YBa_2Cu_3O_7$; the reflection was almost specular up to 600 cm^{-1} and became more and more diffuse at larger frequencies. At room temperature the specular reflectivity decreased from ~0.9 at 50 cm^{-1} to 0.6 at 600 cm^{-1}; the diffuse reflectivity had a value slightly larger than 0.5 at 1000 cm^{-1}. There is a weak phonon structure with five clearly seen resonances. Toward lower temperatures the reflectivity increases; the shape is almost unchanged down to a temperature of 100 K. At very low temperatures ($T \ll T_c$, 20-K curve) the shape is different. On the average, the low-temperature reflectivity is, in comparison with the reflectivity at 100 K, enhanced for $\nu < 380$ cm^{-1} and lowered for larger frequencies. This behavior indicates that the superconductivity has a strong influence on the dynamic conductivity for far-infrared radiation. Most of the phonon structure appears in the form of reflection minima and gives rise to a few other crossing points between the reflectivity curves. We found that reflectivity curves for temperatures below T_c (≃86 K) always crossed the 100-K curve at 380 cm^{-1}.

We have already noted that we have an uncertainty in the absolute values of the reflectivity. Since the reflectivity at 20 K is almost constant for frequencies up to 120 cm^{-1} we suggest that the reflectivity may be almost 1. Our experimental values varied, however, depending on our adjustment, between 0.95 and 1.0. For a further analysis (Subsection 5.A) we assume a value of 1.0. Reflectivity curves at high temperatures ($T \geq T_c$) reported earlier for the same sample[19] were a few percent below the curves of Fig. 11. The discrepancy is most likely an adjustment problem, as we have already mentioned.

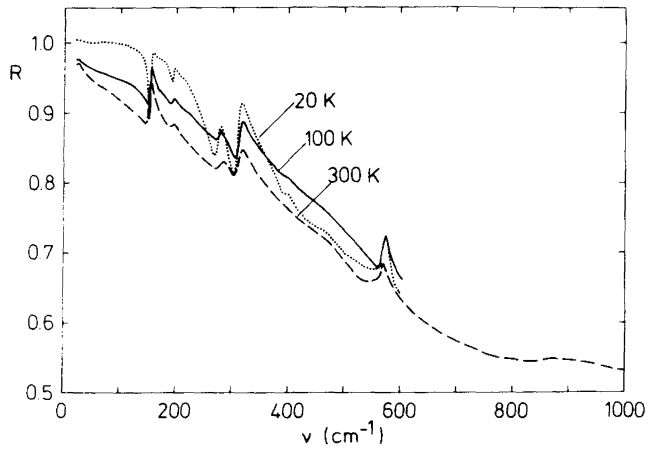

Fig. 11. Far-infrared reflectivity of $YBa_2Cu_3O_7$; specular reflectivity for $\nu \leq 600$ cm^{-1} and the specular plus diffuse reflectivity for $\nu \geq 600$ cm^{-1}.

We found that the reflectivity spectrum for our highly reflecting sample at 20 K was almost unchanged over a period of one year, though the sample was exposed to air most of the time; this shows that the sample's surface region (thickness of a few thousand angstroms) probed by far-infrared radiation was stable. We did not succeed in preparing another $YBa_2Cu_3O_7$ sample of similar high reflectivity. All other samples showed specular reflectivities that decreased strongly with frequency and had values smaller than 0.3 at 600 cm^{-1}; for these samples we usually found a tail of the reflectivity minimum at 153 cm^{-1} toward small frequencies.

B. Far-Infrared Reflectivity of (Nonconducting) Y_2BaCuO_5

For an understanding of phonon spectra of a complicated, sintered cuprate material composed of yttrium, barium, copper, and oxygen we present the far-infrared reflection spectrum of a sintered sample of single-phase (nonconducting) Y_2BaCuO_5; the material has a green color and is present in mixed-phase (green) Y–Ba–Cu–O superconductors.

Figure 12 (upper curve) shows the reflectivity of our sample at a temperature slightly below room temperature. The reflectivity has a rich structure, with sharp maxima and minima. Most prominent are a quite narrow (doublet) resonance near 115 cm^{-1}, a strong reststrahlen band near 310 cm^{-1}, and three other broad resonances near 380, 460, and 530 cm^{-1}. Taking into account our results for larger frequencies (not shown), we find that the phonon spectrum extends up to ~600 cm^{-1}. The reflectivity at small frequencies is almost specular, while scattering sets in near 400 cm^{-1}. Lowering of the temperature leads to a sharpening of the structure and an increase of the reflectivity at small frequencies. From the reflectivities at small frequencies we

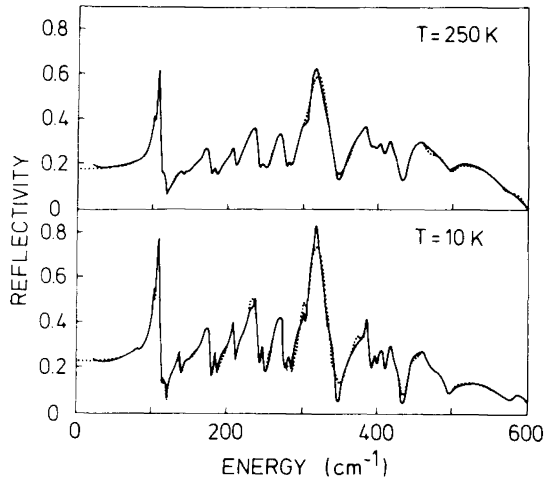

Fig. 12. Far-infrared reflectivity of (nonconducting) Y_2BaCuO_5 and calculated curves (dotted).

find the low-frequency dielectric constants $\epsilon_\rho(250\ \mathrm{K}) \simeq 6.1$ and $\epsilon_\rho(10\ \mathrm{K}) \simeq 6.4$.

We fitted the reflectivity curves by a sum of Lorentzian oscillators according to Eq. (4). We found, by our fitting procedure, that $\epsilon_\infty(250\ \mathrm{K}) \simeq 2.1$ and $\epsilon_\infty(10\ \mathrm{K}) \simeq 2.4$. The real values may be slightly larger since scattering losses at large frequencies are not included in our analysis. The results of our analysis are given in Table 3. For a more-or-less complete fit (dotted lines in Fig. 12) we assumed 28 oscillators.

Following a phonon mode analysis[20] the modes at 102 and 105 cm^{-1} may correspond to vibrations of the heavy barium atoms, the modes at 137, 172, and 184 cm^{-1} to vibrations involving mainly yttrium and copper, and the modes with frequencies above ~250 cm^{-1} most likely to Cu–O vibrations. Further resonances attributed to either $Y_2Cu_2O_5$ or CuO (Ref. 20) were not observed for our sample. A more detailed analysis had to take into account that the sintered material is a composite material consisting of crystallites of different sizes that have different orientations.

We stress that the most prominent reststrahlen structure corresponds to Cu–O vibrations with resonance frequencies of 311 and 301 cm^{-1}. The oscillator strength seems to shift at low temperature from the higher to the lower frequency; this corresponds to frequency shift of an average resonance frequency to smaller values at lower temperatures. We will see that this mode that leads to a strong reststrahlen band at a frequency slightly above 300 cm^{-1} seems to be typical for cuprates, at least for those discussed in this paper.

C. Reflectivity of a Mixed Phase Y-Ba-Cu-O Sample

We studied reflection properties of a mixed phase, with the nominal composition $Y_{1.2}Ba_{0.8}CuO_x$, corresponding approximately to a phase mixture $4Y_2BaCuO_5$:$1YBa_2Cu_3O_7$. The sample had a specific resistance (0.2 mΩ cm) that remained almost constant up to the superconducting transition at 88 K; the width of the transition was ~7 K, and the sample became fully superconducting at 75 K.[18] The reflectivity (Fig. 13) shows almost the same sharp structure as was found for the single-phase Y_2BaCuO_5 sample. There is, however, a background that we attribute to the conducting $YBa_2Cu_3O_7$ phase. This background reflectivity increases toward small frequencies; the low-frequency reflectivity is few percent larger at 10 K than at 100 K.

For a description of the reflectivity R of the mixed-phase sample we write $R = (4/5)R_1 + \Delta R$, where R_1 is the reflectivity of Y_2BaCuO_5 and ΔR is the contribution by the conducting phase. We find, by subtracting from the measured reflectivity R the pure lattice contribution $(4/5)R_1$, where $R_1(\nu)$ is known from a direct measurement (Fig. 12), that the

Table 3. Infrared-Active Phonons of (Nonconducting) Y_2BaCuO_5[a]

250 K (cm^{-1})			10 K (cm^{-1})		
ν_j (cm^{-1})	S_j	Γ_j (cm^{-1})	ν_j (cm^{-1})	S_j	Γ_j (cm^{-1})
102.0	0.3	3.1	101.9	0.7	2.9[a]
105.3	0.5	2.0	105.1	0.7	1.8[a]
114	0.14	7.3	115	0.1	6
137	0.02	3	137	0.07	2[a]
146	0.01	2	146	0.01	2
172.7	0.25	8.4	172.0	0.57	9.8[a]
183.7	0.02	2.6	183.8	0.03	2[a]
207.4	0.13	7.0	207.9	0.21	4[a]
231.9	0.47	13.9	230	0.1	5
235.4	0.06	5.5	234.1	0.5	6[a]
247.3	0.03	5.4	246.5	0.1	7
268.8	0.34	11.7	266.6	0.7	15[a]
282.4	0.02	3.3	282.3	0.02	2.5
301	0.09	8	301	0.3	6
310	0.8	14	309	0.5	8.6[a]
340	0.02	15	342	0.01	8
369	0.4	30	367.7	0.3	26
378.9	0.03	11	382	0.02	6.4[a]
393.3	0.01	9	395	0.007	3
401.1	0.07	20	402	0.04	10[a]
413	0.03	9	414	0.05	12[a]
422	0.01	9	427	0.005	8
445	0.1	21	445	0.04	11[a]
457	0.01	20	454	0.08	21
474	0.07	37	476	0.03	24
504	0.03	26	508	0.01	16[a]
527	0.07	60	530	0.13	75
573	0.005	24	583	0.01	24
$\sum S_j$	4.0			4.0	

[a] Also reported in Ref. 20.

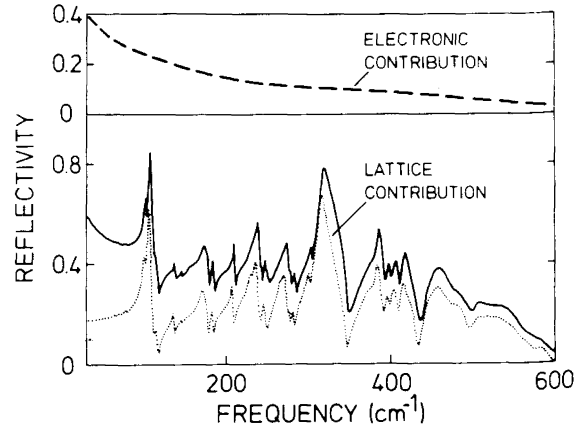

Fig. 13. Reflectivity of a mixed-phase superconductor ($4Y_2BaCuO_5$:$1YBa_2Cu_3O_7$).

contribution ΔR has a value of ~ 0.4 at 50 cm^{-1} and decreases almost smoothly toward larger frequencies (Fig. 13, top).

We note that we could not reproduce the experimental reflectivity curve by a model calculation in which we added dielectric functions for the two phases. In particular, the minima in the theoretical reflection curves were smeared out.[18] Although addition of reflectivities is not a well-founded procedure, we suggest that it is qualitatively justified: We attribute the additional reflectivity ΔR to a contribution from a conducting network of conducting filaments. By comparison of ΔR with reflectivity curves that are known for two-dimensional metallic mesh,[43] we find a typical distance of conducting filaments of the order of 0.1 mm. This is consistent with visual inspection of our sample. A mesh-like (three-dimensional) structure, with a higher conductivity at low temperatures, that is embedded in nonmetallic material is also consistent with the observed increase of reflectivity toward low temperatures (Fig. 13).

D. Reflectivity of a Mixed Phase Y-Ba-Cu-O Thin Film

Thin films of Y–Ba–Cu–O material were produced by a laser evaporation technique.[44,45] A pulsed Nd:YAG laser (wavelength 1.06 μm, pulse duration 50 nsec) with a pulse energy of 0.4 J was used for evaporation of material from a stoichiometric $YBa_2Cu_3O_7$ sample onto a sapphire substrate. The target and the substrate (distance 2 cm) were mounted in a vacuum box (10^{-5} Torr); the substrate was heated to 400°C. The target was rotated during laser processing. After evaporation, films were annealed in an oxygen atmosphere at high temperatures.

A Rutherford backscattering analysis indicated that the stoichiometry of the film was slightly yttrium rich and barium deficient; a composition $Y_{1.3}Ba_{1.8}Cu_3$ was measured. X-ray diffraction measurements yielded diffraction patterns similar to those of polycristalline $YBa_2Cu_3O_7$ samples,[46] indicating that the film consisted mainly of the superconducting phase. Scanning electron micrographs showed that the film surface contained grains 1 to 10 μm in size. One of our (hitherto best) films showed the onset of superconductivity at 100 K, T_c values of 94–76 K (90–10%), and zero resistance at 50 K (Fig. 14, inset). Reflectivity measurements for this film are shown in Fig. 14. The reflectivity is high at small frequencies, decreases strongly toward larger frequencies, and shows phonon structure. The overall behavior of the normal state reflectivity (without phonon structure) can be qualitatively described by the Drude dynamic conductivity and, additionally, by assuming scattering at the film surface at large frequencies (>300 cm^{-1}). At small frequencies the reflectivity is, however, slightly higher than that calculated with a Drude model, and it increases slightly(by $\sim 4\%$) when the sample is cooled below T_c; a crossing of the 20-K curve with the 110-K curve occurs between 300 and 400 cm^{-1}. The behavior is qualitatively the same as for the bulk sample. All structures were also observed, at the same frequencies, for films evaporated with the same technique on $SrTiO_3$ substrates.

Although the film is conducting, its reflectivity shows strong structure. There is a pronounced reststrahlenlike band near 320 cm^{-1}. The shape and the temperature dependence strongly resemble those found for single-phase Y_2BaCuO_5 (Fig. 12). A detailed comparison of the spectra shows that almost all structure found for Y_2BaCuO_5 occurs in the film spectra of Fig. 14. While the structure at larger frequencies is strong, it becomes weaker at smaller frequencies; i.e., at smaller frequencies metalliclike conductivity mainly determines the reflection properties; suppression of phonon resonance is best seen for the resonance near 105 cm^{-1}. Also seen in the reflection spectra of the film are (weak) resonances that are characteristic of $YBa_2Cu_3O_7$. For a more detailed discussion we performed a Kramers–Kronig analysis. We found that almost all resonances of bulk Y_2BaCuO_5 (Table 3) appeared. The resonances of bulk $YBa_2Cu_3O_7$ (Table 4) were also found, however (slightly shifted), namely, at 150 cm^{-1} (instead of 153 cm^{-1}), 270 cm^{-1} (280 cm^{-1}), and 314 cm^{-1} (308 cm^{-1}); the 192-cm^{-1} resonance is indicated only as a shoulder. Few resonances are narrow ($\Gamma_j \simeq 5$ cm^{-1} for the 207-, 282-, and 301-cm^{-1} modes), and most are broad (typically $\Gamma_j \simeq 15$ cm^{-1}).

Our analysis of the far-infrared reflection spectrum suggests, in reasonable agreement with the Rutherford backscattering analysis, that the film was a mixed-phase sample with the approximate molecular composition $4YBa_2Cu_3O_7{:}1Y_2BaCuO_5$. The reflectivity spectrum at large frequencies shows a strong structure that corresponds to the reststrahlen band of the nonconducting phase, whereas metalliclike reflection with weaker structure is observed at small frequencies. These results demonstrate that a large portion of the reflection occurs at the nonconducting phase even if its concentration is noticeably smaller than that of the conducting phase; a discussion of a mixed phase consisting of nonconducting material embedded in a conducting network is presented in Subsection 5.C.

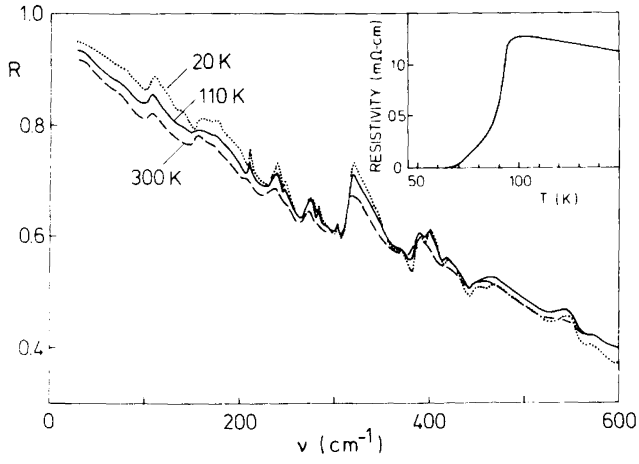

Fig. 14. Reflectivity of a thin film ($4YBa_2Cu_3O_7{:}1Y_2BaCuO_5$) on a sapphire substrate; insert, film resistivity.

Table 4. Infrared-Active Phonons for $YBa_2Cu_3O_7$

	ν_j (cm^{-1})			S_j		Γ_j (cm^{-1})		
j	10 K		110 K	10 K	110 K	10 K		110 K
1	–	153	–	3	5	4	–	7
2	–	192	–	0.5	0.5	–	10	–
3	276		278	1	0.8	–	15	–
4	308		312	1.5	1.3	–	15	–
5	565		567	0.23	0.19	–	20	–

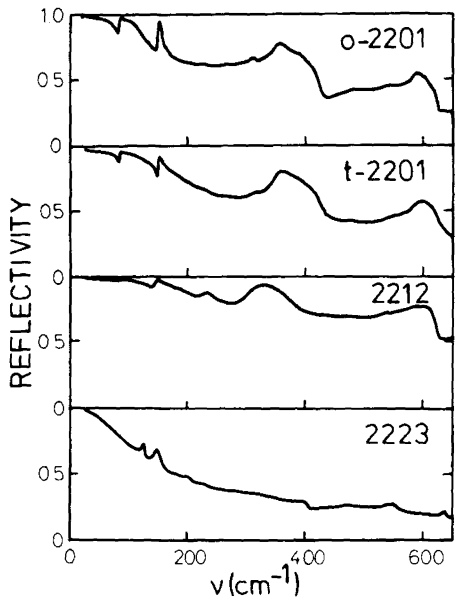

Fig. 15. Far-infrared reflectivity of the $Tl_2Ba_2Ca_nCu_{n+1}O_{2n+6}$ (n = 0, 1, 2) series at low temperature ($T < 50$ K).

E. Reflectivity of $Tl_2Ba_2Ca_nCu_{n+1}O_{2n+6}$ (n = 0, 1, 2) Series

For a survey we show in Fig. 15 the far-infrared reflectivity spectra of the homologous series $Tl_2Ba_2Ca_nCu_{n+1}O_{2n+6}$ (n = 0, 1, 2) for low temperatures. Common to all phases are a high reflectivity at small frequencies, a decrease toward large frequencies, and, furthermore, a pronounced phonon structure. The reflectivity of the 2201 phases and the 2212 phase remains quite high at large frequencies, corresponding to a high surface quality that was obtained without further treatment of the samples after sintering. The decrease of reflectivity of the 2223 phase is due to a larger surface roughness. The surface of the 2223 phase sample was finished by grinding (necessary for removing foreign phases; see Subsection 2.F). Without grinding, however, the 2223 phase samples showed an even smaller reflectivity with a slightly more pronounced structure than after grinding; this is a consequence of decomposition during heat treatment in air, which was necessary to obtain the 2223 phase (see Subsection 2.F). We note that the reflectivity curves for the $Tl_2Ba_2Ca_nCu_{n+}O_{2n+6}$ samples were almost the same for different samples prepared in the same way.

There are two resonancelike reflection minima (at 78 and 142 cm^{-1}) that are strong for the o-2201 phase, weaker for the t-2201 phase, and still weaker for the 2212 phase. We attribute the minima to a thallium vibration (against the rest of the lattice) or to a barium vibration, with elongations along the c axis; the barium vibration seems to be slightly softer than for $YBa_2Cu_3O_7$ (at 152 cm^{-1}). For the 2223 phase, resonances are found at different frequencies (113 and 134 cm^{-1}).

Most remarkable are two strong reststrahlen bands (Fig. 15), namely, a high-frequency band that appears for the 2201 and 2212 phases in the same frequency range and a low-frequency band at a slightly smaller frequency for the 2212 phase than for the 2201 phases; evidence is found for a weak low-frequency band for the 2223 phase (lowest curve of Fig. 15).

Reflectivity curves for different phases at different temperatures are shown in Figs. 16–19. Besides the two strong narrow phonon resonances (at 78 and 142 cm^{-1}) there are further weak resonances (at 226 cm^{-1} for the 2212 phase and at 200 cm^{-1} for the 2223 phase) seen at all temperatures and a narrow resonance (at 318 cm^{-1}) that appears for the 2201 phases at low temperatures only (<200 K). The highest overall reflectivity is found for the 2212 phase (Fig. 18). The phonon structure is well pronounced and becomes most significant at low temperatures, although the background reflectivity is higher than at high temperatures. The high-frequency reststrahlen band clearly shows a reflection minimum at 630 cm^{-1} that is almost independent of temperature; we suggest that this frequency corresponds to a longitudinal optic mode. Toward larger frequencies the (diffuse) reflectivity (Fig. 18, inset) decreases smoothly. High specular reflectivity (0.16 at 5000 cm^{-1}) is a measure of high surface quality in the sample studied.

The influence of superconductivity is not seen for the t-2201 phase (Fig. 17). The reflectivity below T_c ($\simeq$54 K) is almost the same as above T_c; the change of reflectivity at low temperatures is similar to that for the (nonsuperconducting) o-2201 phase. An influence of superconductivity is found for the 2212 phase. Below T_c ($\simeq$105 K) the reflectivity is enhanced in almost the whole frequency range up to 900

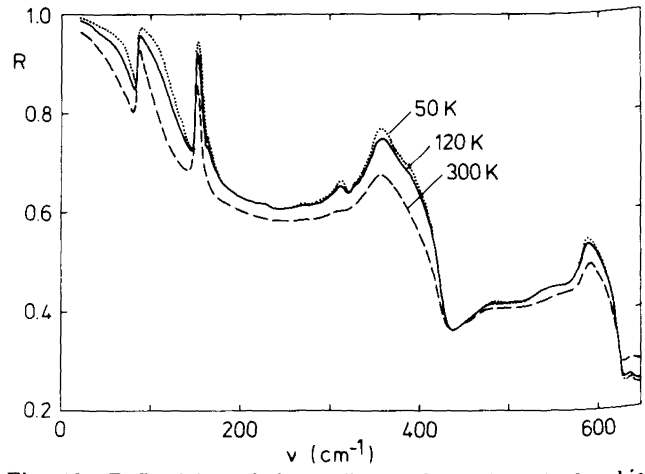

Fig. 16. Reflectivity of (normally conducting) orthorhombic $Tl_2Ba_2CuO_6$.

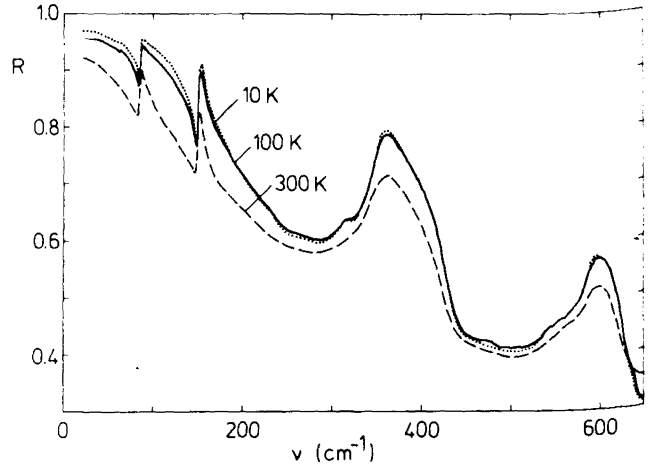

Fig. 17. Reflectivity of tetragonal $Tl_2Ba_2CuO_6$ ($T_c \simeq 54$ K).

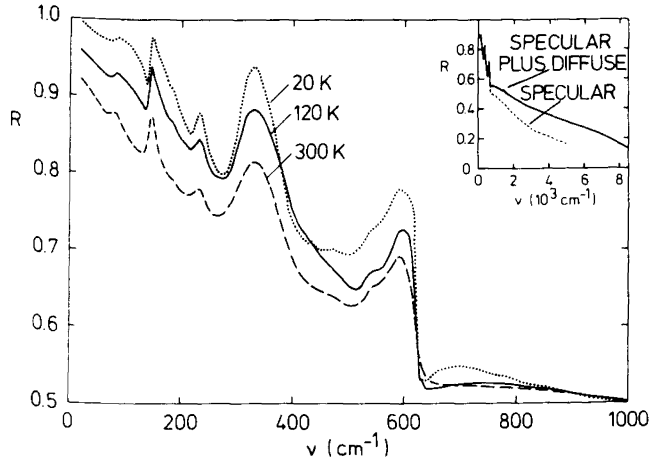

Fig. 18. Far-infrared reflectivity of $Tl_2Ba_2CaCu_2O_8$ ($T_c \simeq 105$ K) and infrared reflectivity (inset).

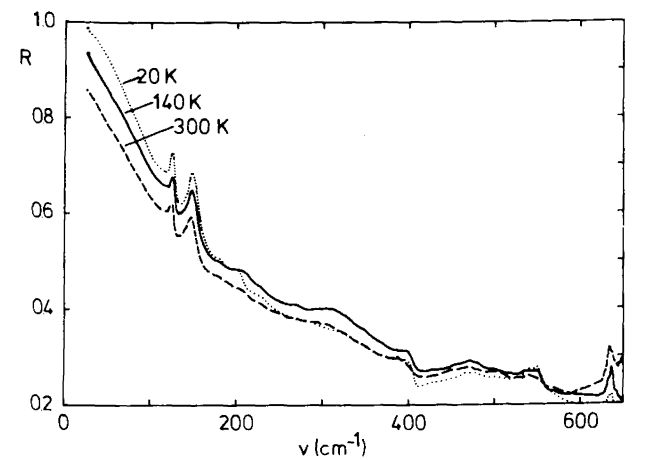

Fig. 19. Reflectivity of $Tl_2Ba_2Ca_2Cu_3O_{10}$ ($T_c \simeq 110$ K).

cm^{-1}. Maximum enhancement occurs near 500 cm^{-1}; from this, an energy gap of $2\Delta/kT_c \simeq 5$ may be suggested. For the 2223 phase, enhancement of reflectivity at low temperatures is found (Fig. 18) for small frequencies ($\leq$300 cm^{-1}).

5. ANALYSIS AND DISCUSSION

A. Dynamic Conductivity of $YBa_2Cu_3O_7$

For $YBa_2Cu_3O_7$ the reflectivity at large frequencies can be described by a Drude conductivity according to Eq. (3) and by a bound-electron conductivity according to relation (6), with $\sigma_n \simeq 5.4 \times 10^4\ \Omega^{-1}\ m^{-1}$, $\nu_\tau \simeq 15\,000\ cm^{-1}$, $\nu_p \simeq 20\,000$ cm^{-1}, and $\epsilon_\infty \simeq 2$. σ_n is an order of magnitude smaller than the dc conductivity at 300 K. We performed a Kramers–Kronig analysis of our reflectivity data and obtained (Fig. 20) apparent conductivities, i.e., conductivities that follow by application of the homogeneous-medium theory. At room temperature (two top panels) the real part, σ_1, shows a broad minimum, with a value that is smaller than $(1/2)\sigma_n$, and increases toward small frequencies (being constant at very small frequencies), and the imaginary part shows large values at small frequencies ($\sigma_2 \to 0$ for $\nu \to 0$). This behavior is not Drude-like. Toward lower temperatures (for $T > T_c$), the deviation from a Drude behavior increases. For low temperatures ($T \ll T_c$), σ_1 becomes small (or negligible) at small frequencies, and (if the phonon structure is neglected) σ_2 increases strongly toward small frequencies. The behavior at low temperatures gives evidence for the behavior expected from the Mattis–Bardeen theory, with a superconducting energy gap near 300 cm^{-1} ($2\Delta/kT_c \simeq 5$). A more detailed analysis[19] yielded a distribution of energy gaps ($2.2 \leq 2\Delta/kT_c \leq 7$). The result is also consistent with two energy gaps defined by tunnel measurements (Subsection 2.C). An increase of σ_1 and σ_2 near 100 K, for small frequencies, may be attributed to superconducting fluctuations.[19]

There are five pronounced phonon resonances. If we describe the resonances by Lorentzian oscillators according to Eq. (4), we obtain the parameters summarized in Table 4. The $j = 1$ mode, most likely caused by a barium vibration against the other ions, narrows at temperatures below T_c. This indicates that the damping is reduced when the phonon energy is not sufficient to break up Cooper pairs. The $j = 1$ mode is five times stronger than corresponding modes in the nonconducting Y_2BaCuO_5 (Table 3). The $j = 4$ mode that can be attributed to a Cu–O vibration softens (continuously) with decreasing temperature (from 315 cm^{-1} at 300 K to 308 cm^{-1} at 20 K). This mode most likely corresponds to the strong modes at 304 and 301 cm^{-1} (Table 3) responsible for the strongest reststrahlen band for Y_2BaCuO_5 (Fig. 12).

Several questions remain: (1) Why does σ_1 (at room temperature) show a minimum in the range of infrared active phonons? (2) Why does the $j = 1$ mode of $YBa_2Cu_3O_7$ have an oscillator strength that is much larger than that of comparable modes of Y_2BaCuO_5, and why is the strength strongly dependent on temperature? We discuss these points in Subsection 5.C below.

B. Dynamic Conductivity of $Tl_2Ba_2CaCu_2O_8$

The (diffuse) reflectivity for large frequencies (Fig. 18, inset) can be described by Drude conductivity according to Eq. (3) and by bound-electron conductivity according to relation (6), with $\sigma_n \simeq 6 \times 10^4\ \Omega^{-1}\ m^{-1}$, $\nu_\tau \simeq 9000\ cm^{-1}$, $\nu_p \simeq 18\,000$ cm^{-1}, and $\epsilon_\infty \simeq 2$; these values are similar for $YBa_2Cu_3O_7$. The conductivity σ_n is a factor of 5 smaller than the dc conductivity at room temperature.

The result of a Kramers–Kronig analysis of reflectivity curves is shown in Fig. 21. The conductivity curves show strong phonon structure. If we describe the phonon struc-

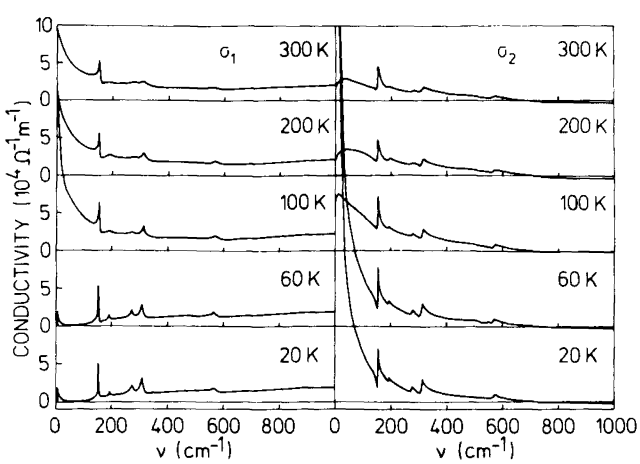

Fig. 20. Apparent dynamic conductivity of $YBa_2Cu_3O_7$.

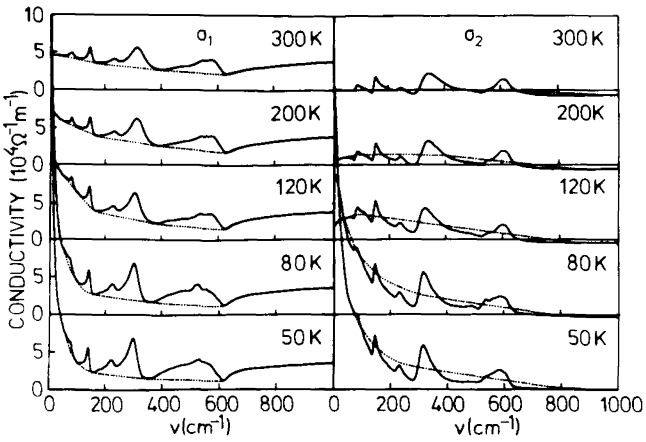

Fig. 21. Apparent dynamic conductivity of $Tl_2Ba_2CaCu_2O_6$.

ture by Lorentzian resonance curves according to Eq. (4), we obtain the dotted curves of Fig. 21 for the real part, σ_1^c, and the imaginary part, σ_2^c, of the charge-carrier conductivity. The real part is not a constant, i.e., is not Drude-like, even at high temperatures, but shows a broad minimum in the range of the phonon resonances. For lower temperatures the minimum becomes more pronounced. At low temperatures σ_1^c increases strongly with decreasing frequency and reaches values larger than σ_n. The imaginary part, σ_2^c, is almost zero at high temperature and increases, mainly at low frequencies, toward low temperatures. The strong increase of σ_2^c with decreasing temperature found for $T < T_c$ gives evidence of the influence of superconductivity on the dynamic conductivity. However, no conclusion can be drawn with respect to an energy gap.

A description of the narrow resonances (Fig. 21) by Lorentzian oscillators according to Eq. (4) results in the data of Table 5. We find seven infrared-active phonon modes. As we have already mentioned, we attribute the $j = 1$ mode to a thallium vibration, the $j = 2$ mode to a barium vibration, and the other modes to Cu–O vibrations. The damping of the modes increases with increasing resonance frequency; the $j = 2$ mode becomes narrower at low temperatures. The most prominent mode, $j = 4$ (near 300 cm^{-1}) nearly coincides with corresponding modes for $YBa_2Cu_3O_7$ (Table 4) and Y_2BaCuO_5 (Table 3) and shows a temperature dependence similar to those of these modes. According to reflection data (Fig. 15), the same mode appears to lie ~10% higher in the 2201 thallium compounds. Thus the mode near 300 cm^{-1} seems to be characteristic of the cuprates, at least for those studied in the research presented in this paper. It is unclear whether this Cu–O vibration plays a direct role in the occurrence of high-T_c superconductivity.

Our analysis produces anomalously large values of S_j, i.e., the oscillator strength of the barium vibration ($j = 2$ mode, Table 5) is an order of magnitude larger than oscillator strengths for low-frequency modes in Y_2BaCuO_5 (Table 3), and the strength of the Cu–O resonance near 300 cm^{-1} seems to be more than an order of magnitude larger than for Y_2BaCuO_5. Furthermore, the $j = 7$ resonance is expected, according to the Lyddane–Sachs–Teller relation, to have a longitudinal optic phonon frequency of 710 cm^{-1} (for $\epsilon_\infty = 2$); such a frequency is extremely high. Finally, according to our analysis, the static dielectric constant $\epsilon_s = \epsilon_\infty + \sum S_j$ would be almost an order of magnitude larger than for Y_2BaCuO_5 and would be strongly temperature dependent; with $\epsilon_\infty = 2$ we find that $\epsilon_s(300\ K) \simeq 38$, $\epsilon_s(120\ K) \simeq 42$, and $\epsilon_s(50\ K) \simeq 58$.

The analysis of the reflectivity spectra of $Tl_2Ba_2CaCu_2O_8$ (and of the other members of the series) raises questions similar to those for the analysis of $YBa_2Cu_3O_7$, namely: Why does the real part of σ_1 show a minimum; why are the oscillator strengths of the phonons anomalously large, and why do they increase strongly with decreasing temperature? A further discussion is given in Subsection 5.C.

C. Network Theory for Conducting Ceramics

The results above show that linear addition of a phononic and an electronic conductivity, i.e., treatment of the metal–ceramic materials as a homogeneous material, does not lead to a simple and consistent description of the far-infrared reflectivity of $YBa_2Cu_3O_7$ and $Tl_2Ba_2CaCu_2O_8$ (and of the other members of the $Tl_2Ba_2Ca_nCu_{n+1}O_{2n+6}$ series). We have tried to modify the analysis by using the so-called effective-medium theory[47] when two conductivities are mixed in a complicated way. However, this procedure did not produce a satisfactory description of the far-infrared reflectivity either; in this theory, the structure in the reflectivity spectra becomes almost smeared out.

The experimental reflectivity spectra, in particular those for the 2201 and 2212 phases of the thallium compounds (Figs. 16–18), show well-pronounced phonon structure with reststrahlen behavior at large frequencies typical for insulating material and, on the other hand, a high background reflectivity characteristic for material of high charge-carrier conductivity. The behavior at large frequencies would seem to indicate that we could add reflectivities of insulating and conducting parts. Such a description is, however, too naïve, because it does not deliver a reflectivity close to 1 at small frequencies; furthermore, the narrow phonon resonances with reduction of reflectivity at small frequencies cannot be explained. A possible solution of this puzzle may be obtained by taking into account that the conducting grains are connected continuously, establishing a three-dimensional network (as indicated by an isotropic dc conductivity) that contains insulating material in the holes; a characteristic diameter of the holes may correspond to the grain size (typically of the order of 10 μm). Then, at small frequencies where the wavelength of the infrared radiation is large compared with the grain size, reflection occurs mainly at the metallic network; at larger frequencies where the wavelength is comparable with the size of the grains, the radiation can penetrate into the holes of the network and can be

Table 5. Infrared-Active Phonons of $Tl_2Ba_2CaCu_2O_8$ for 300 K (and 20 K)

j	ν_j (cm^{-1})	S_j	Γ_j (cm^{-1})
1	75	11	10
2	142	7 (13)	20 (10)
3	222	2 (5)	30
4	311 (302)	10 (16)	45
5	460	1 (3)	50
6	520	2 (4)	70
7	565	3 (4)	70
		$\sum S_j$ 36 (56)	

reflected mainly at the nonmetallic material, giving rise to reststrahlenlike reflectivity.

To illustrate this view we have performed a model calculation, assuming that a metal–ceramic sample can be represented by a thick plate of perfectly conducting material with holes filled with insulating material. Such structures are described in the literature as filters for far-infrared radiation. Large-wavelength radiation cannot penetrate into the holes and becomes reflected, while small-wavelength radiation can penetrate and is partly reflected and, if the insulating material is nonabsorbing, is partly transmitted; diffraction can occur, too. The penetration of radiation into the holes can be described by a complex wave vector $k = n\omega/c$, where the complex refractive index n is related to the complex dielectric function ϵ of the filling material by[48]

$$n^2 = \epsilon - \nu_c^2/\nu^2, \tag{9}$$

where $\nu_c = A/d$ is a characteristic frequency, d is the diameter of the holes, and A is a constant of the order of 1 ($A = 0.56$ for the TEM_{11} mode). Equation (9) describes the property of the whole plate if it is assumed that the holes are separated from one another by thin conducting walls. When finite lateral extension of the conducting material was taken into account, the theory had to be modified. We now assume for simplicity that a portion of incident radiation is directly reflected at the surface of the conducting material while another portion penetrates into the holes. For a calculation we assume that two thirds of the incident radiation intensity is directly reflected, i.e., that two thirds of the material surface is ideally conducting. We then describe the rest of the radiation, which penetrates into the holes, by Eq. (9). We assume a hole diameter $d \simeq 10\ \mu$m, i.e., $\nu_c \simeq 560\ \text{cm}^{-1}$, and take into account two phonon resonances that we describe by Eq. (4), with eigenfrequencies $\nu_1 = 150\ \text{cm}^{-1}$ and $\nu_2 = 570\ \text{cm}^{-1}$, strengths $S_1 = S_2 = 0.8$, and relative damping constants $\Gamma_1/\nu_1 = \Gamma_2/\nu_2 = 0.05$. With $\epsilon_\infty = 4$, we obtain the curve of Fig. 22. At small frequencies the reflectivity is almost 1 and shows a sharp cutoff at the cutoff frequency $\nu_c/n \simeq 250\ \text{cm}^{-1}$. The phonon resonance with a resonance frequency below the cutoff frequency appears as a sharp dip in the reflectivity curve, while the phonon resonance above the cutoff leads to a typical broad reststrahlen band with a steep rise of reflectivity at the resonance frequency and a steep decrease near the longitudinal optic frequency $\nu_{2,l}$ ($\simeq 630\ \text{cm}^{-1}$), which follows from the Lyddane–Sachs–Teller relation $\nu_{2,l}^2 = \nu_2^2(\epsilon_\infty + S_2)/\epsilon_\infty$; note that a temperature dependence of the damping of the oscillators leads to a change of the structure of the reflectivity spectrum.

Although our theoretical treatment has a rather qualitative character, the theoretical curve (Fig. 22) shows the main features of experimental reflectivity curves. A comparison with experimental results for the 2201 and 2212 phases of the $Tl_2Ba_2Ca_nCu_{n+1}O_{2n+6}$ series (Figs. 16–18) suggests a cutoff frequency near 200 cm^{-1} (as assumed in our example of Fig. 22), corresponding to a characteristic dimension of nonconducting areas of the order of 10 μm. These nonconducting areas may correspond to crystallites with the c axis in the sample plane. Our calculation then holds for the electric field vector of the radiation parallel to the c axis. In this direction the dynamic conductivity is most likely negligibly small. In a statistical arrangement of crystallites one third of the electromagnetic wave would hit nonconducting material (as assumed in our example). Sharp reflection dips at small frequencies and reststrahlen bands at larger frequencies are described well by our theory. Thus our analysis reproduces the main structure of the far-infrared reflectivity spectra, and it leads to strengths S_j (<1) that seem to be much more realistic (for instance, if compared with values for Y_2BaCuO_5) than those obtained with the homogeneous-medium theory (Table 5).

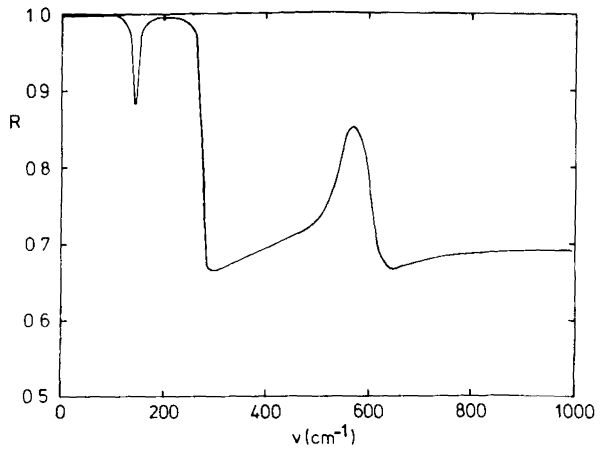

Fig. 22. Calculated far-infrared reflectivity for a conducting network containing nonconducting material.

We also apply the theory to the single-phase ceramic $YBa_2Cu_3O_7$ sample (Fig. 11) and find a strength $S_1 \approx 0.2$ (and $S_2 \approx 0.02$); for the other modes $S_j \approx 0.5$ may be suggested. It follows, by using the Lyddane–Sachs–Teller relation (and taking $\epsilon_\infty = 4$), that the corresponding $j = 1$ longitudinal mode has a frequency $\nu_{1,l} \approx 164\ \text{cm}^{-1}$. We know that an earlier lattice dynamic calculation (for $YBa_2Cu_3O_6$) delivered[49] $\nu_1 = 153\ \text{cm}^{-1}$ and $\nu_{1,l} = 163\ \text{cm}^{-1}$ for the barium mode. A larger but narrower dip at 153 cm^{-1} for another $YBa_2Cu_3O_7$ sample,[50] which showed slightly higher reflectivity than our sample, is fully consistent with our analysis (and with $S_1 \approx 0.2$).

We stress that the reflectivity behavior of mixed-phase samples (Subsections 4.B and 4.C) is fully consistent with our analysis.

Our theory can be improved in several ways. First, we can introduce more than two resonances. Then, we can take into account finite conductivity, which leads to a frequency-dependent modification of the reflectivity of the metallic network (including the background reflectivity). At high temperatures, description by Drude conductivity, and at low temperatures ($T < T_c$), description by Mattis–Bardeen conductivity may now lead to a consistent description of the free-charge-carrier conductivity. For a more quantitative description of the experimental results a distribution of various hole diameters (and also of hole shapes) may be necessary. Finally, in a more elaborate theory we must take into account appropriate boundary conditions for the electromagnetic waves incident upon the metallic network.

6. CONCLUSIONS

We have presented a systematic investigation of ceramic high-T_c materials and related materials. We described procedures that we used for sample preparation, and we presented results of a careful analysis by x-ray diffraction meth-

ods that allowed us to determine structure and phase composition. We reported on various techniques, such as electric, magnetic, tunnel, and Raman experiments, for a basic characterization of the materials. We discussed far-infrared reflection measurements with the aim of determining the dynamic conductivity that is related to free charge carriers, and therefore to superconductivity, and to obtain information on phonons. Besides a general survey of the far-infrared reflection behavior of (complicated) ceramic materials, we presented a detailed analysis and comparison of the reflection data for single-phase samples of (nonconducting) Y_2BaCuO_5 and (conducting) $YBa_2Cu_3O_7$ and $Tl_2Ba_2CaCu_2O_8$. The similarity of prominent phonon structure occurring in all three compounds leads us to suggest that the far-infrared reflectivity of ceramic conductors, with statistical arrangement of crystallites that show conductivity in the plane perpendicular to the c axis but almost no conductivity along the c axis, is determined mainly by the geometric structure of the material: a conducting three-dimensional network that contains nonconducting material. At small and large frequencies the conducting network mainly determines the reflectivity, while in the range of the reststrahlen bands the nonconducting material leads to pronounced phonon structure. A theoretical treatment indicates that the shape of the phonon structure depends sensitively on the geometric dimensions of the conducting network. Our analysis gives evidence that $YBa_2Cu_3O_7$ and $Tl_2Ba_2CaCu_2O$ have superconducting energy gaps, with $2\Delta/kT_c \simeq 5$, and that, possibly, distributions of energy gaps occur.

ACKNOWLEDGMENTS

We thank U. Schröder and D. Strauch for helpful discussions. The research was supported by the Bundesministerium für Forschung und Technologie, Federal Republic of Germany.

REFERENCES

1. J. G. Bednorz and K. A. Müller, Z. Phys. B **64,** 189 (1986).
2. M. K. Wu, J. Ashburn, C. J. Torng, P. H. Hor, R. L. Meng, L. Gao, Z. J. Huang, Y. Q. Wang, and C. W. Chu, Phys. Rev. Lett. **58,** 908 (1987).
3. C. Michel, M. Hervieu, M. M. Borel, A. Grandin, F. Deslandes, J. Provost, and B. Raveau, Z. Phys. B **68,** 421 (1987).
4. C. W. Chu, J. Bechtold, L. Gao, P. H. Hor, Z. J. Huang, R. L. Meng, Y. Y. Sun, Y. Q. Wang, and Y. Y. Xue, Phys. Rev. Lett. **60,** 941 (1988).
5. H. G. von Schnering, L. Walz, M. Schwarz, W. Becker, M. Hartweg, T. Popp, B. Hettich, P. Müller, and G. Kämpf, Angew. Chem. **100,** 604 (1988).
6. J. L. Tallon, R. G. Buckley, P. W. Gilberd, M. R. Presland, I. W. M. Brown, M. E. Bowden, L. A. Christian, and R. Goguel, Nature **333,** 153 (1988).
7. Z. Z. Sheng and A. M. Hermann, Nature **332,** 55, 138 (1988).
8. G. A. Thomas, H. K. Ng, A. J. Millis, R. N. Bhatt, R. J. Cava, E. A. Rietman, D. W. Johnson, Jr., G. P. Espinosa, and J. M. Vanderberg, Phys. Rev. B **36,** 846 (1987).
9. D. A. Bonn, J. E. Greedan, C. V. Stager, T. Timusk, M. G. Doss, S. L. Herr, K. Kamarás, and D. B. Tanner, Phys. Rev. Lett. **58,** 2249 (1987).
10. L. Genzel, A. Wittlin, A. Kuhl, Hj. Mattausch, W. Bauhofer, and A. Simon, Solid State Commun. **63,** 843 (1987).
11. S. Onari, M. Iioka, K. Ohshima, T. Arai, and T. Sakudo, Jpn. J. Appl. Phys. **26,** L1052 (1987).
12. R. T. Collins, Z. Schlesinger, R. H. Koch, R. B. Laibowitz, T. S. Plaskett, P. Freitas, W. J. Gallagher, R. L. Sandstrom, and T. R. Dinger, Phys. Rev. Lett. **59,** 704 (1987).
13. J. M. Wrobel, S. Wang, S. Gygax, B. P. Clayman, and L. K. Peterson, Phys. Rev. B **36,** 2368 (1987).
14. P. Sulewski, T. W. Noh, J. T. McWhirter, A. J. Sievers, S. E. Russek, R. A. Buhrman, C. S. Jee, J. E. Crow, R. E. Salomon, and G. Meyer, Phys. Rev. B **36,** 2357 (1987).
15. T. W. Noh, P. E. Sulewski, and A. J. Sievers, Phys. Rev. B **36,** 8866 (1987).
16. A. Wittlin, R. Liu, M. Cardona, L. Genzel, W. König, W. Bauhofer, Hj. Mattausch, and A. Simon, Solid State Commun. **64,** 477 (1987).
17. Z. Schlesinger, R. T. Collins, D. L. Kaiser, and F. Holtzberg, Phys. Rev. Lett. **59,** 1958 (1987).
18. K. F. Renk, H. Lengfellner, P. E. Obermayer, W. Ose, H. H. Otto, T. Zetterer, W. Schindler, and G. Saeman-Ischenko, Intl. J. Infrared Millimeter Waves **8,** 1525 (1987).
19. W. Ose, P. E. Obermayer, H. H. Otto, T. Zetterer, H. Lengfellner, J. Keller, and K. F. Renk, Z. Phys. B **70,** 307 (1988).
20. Z. V. Popović, C. Thomsen, M. Cardona, R. Liu, G. Stanisić, and W. König, Solid State Commun. **66,** 43 (1988).
21. M. Udaga, N. Ogita, A. Fukumoto, Y. Utsunomiya, and K. Ohbayashi, Jpn. J. Appl. Phys. **26,** L858 (1987).
22. W. I. F. David, W. T. A. Harrison, J. M. F. Gunn, O. Moze, A. K. Soper, P. Day, J. D. Jorgensen, D. G. Hinks, M. A. Beno, L. Soderholm, D. W. Capone, I. K. Schuller, C. U. Segre, K. Zhang, and J. D. Grace, Nature **327,** 310 (1987).
23. B. G. Hyde, J. G. Thompson, R. L. Withers, J. G. FitzGerald, A. M. Stewart, D. J. M. Bevan, J. S. Anderson, J. Bitmead, and M. S. Paterson, Nature **327,** 402 (1987).
24. H. F. C. Hoevers, P. J. M. van Bentum, L. E. C. van de Leemput, H. van Kempen, A. J. G. Schellingerhout, and D. van der Marel, Physica **C152,** 105 (1988).
25. J. R. Kirtley, R. T. Collins, Z. Schlesinger, W. J. Gallagher, R. L. Sandstrom, T. R. Dinger, and D. A. Chance, Phys. Rev. B **35,** 8846 (1987).
26. M. F. Crommie, L. C. Bourne, A. Zettl, M. L. Cohen, and A. Stacy, Phys. Rev. B **35,** 8853 (1987).
27. N. Hohn, R. Koltun, H. Schmidt, S. Blumenröder, H. General, G. Güntherodt, and D. Wohlleben, Z. Phys. B **69,** 173 (1987).
28. J.-S. Tsai, Y. Kubo, and J. Tabuchi, Jpn. J. Appl. Phys. **26,** L701 (1987).
29. J. Moreland, L. F. Goodrich, J. W. Ekin, T. E. Capobianco, A. F. Clark, A. I. Braginski, and A. J. Pauson, Appl. Phys. Lett. **51,** 540 (1987).
30. J. Niemeyer, N. D. Kataria, M. R. Dietrich, C. Politis, H. Koch, R. Schöllhorn, and H. Eickenbusch, Z. Phys. B **69,** 1 (1987).
31. Y. Higashino, T. Takahashi, T. Kawai, and S. Naito, Jpn. J. Appl. Phys. **26,** L1211 (1987).
32. Xie Sishen, Institute of Physics, Academia Sinica, P.O. Box 603, Beijing, China (personal communication).
33. H. H. Otto, T. Zetterer, and K. F. Renk, Naturwissenschaften **75,** 509 (1988).
34. T. Zetterer, H. H. Otto, G. Lugert, and K. F. Renk, "Crystal chemistry of the $Tl_{2-x}Ba_2Ca_nCu_{n+1}O_{2n+6}$ (n = 0, 1, 2) high-T_c superconductors," Z. Phys. B (to be published).
35. M. A. Subramanian, J. C. Calabrese, C. C. Torardi, J. Gopalakrishnan, T. R. Askew, R. B. Flippen, K. J. Morrissey, U. Chowdhry, and A. W. Sleight, Nature **332,** 420 (1988).
36. L. G. Aslamasov and A. I. Larkin, Phys. Lett. **26A,** 238 (1968).
37. K. A. Müller, M. Takashige, and J. G. Bednorz, Phys. Rev. Lett. **58,** 1143 (1987).
38. B. Renker, I. Apfelstedt, H. Küpfer, C. Politis, H. Rietschel, W. Schauer, H. Wühl, U. Gottwick, H. Kneissel, U. Rauchschwalbe, H. Spille, and F. Steglich, Z. Phys. B **67,** 1 (1987).
39. R. Liu, C. Thomsen, W. Kress, M. Cardona, B. Gegenheimer, F. W. de Wette, J. Prade, A. D. Kulkarni, and U. Schröder, Phys. Rev. B **37,** 7971 (1988).
40. Z. V. Popovic, C. Thomsen, M. Cardona, R. Lin, G. Stanisic, R. Kremer, and W. König, Solid State Commun. **66,** 965 (1988).
41. D. C. Mattis and J. Bardeen, Phys. Rev. **111,** 412 (1958).
42. M. Tinkham, in *Far Infrared Properties of Solids*, S. S. Mitra and S. Nudelman, eds. (Plenum, New York, 1970).
43. K. F. Renk and L. Genzel, Appl. Opt. **1,** 646 (1962).

44. D. Dijkkamp, T. Venkatesan, X. D. Wu, S. A. Shaheen, N. Jisrawi, Y. H. Min-Lee, W. L. McLean, and M. Croft, Appl. Phys. Lett. **51,** 619 (1987).
45. H. Lengfellner, K. F. Renk, P. Fickenscher, and W. Schindler, "Preparation of Y–Ba–Cu–O thin films by laser evaporation with near-infrared radiation," J. Phys. D (to be published).
46. R. Beyers, G. Lim, E. M. Engler, R. J. Savoy, T. M. Shaw, T. R. Dinger, W. J. Gallagher, and R. L. Sandstrom, Appl. Phys. Lett. **50,** 1918 (1987).
47. T. W. Noh, P. E. Sulewski, and A. J. Sievers, Phys. Rev. B **36,** 8866 (1987).
48. F. Keilmann, Intl. J. Infrared Millimeter Waves **2,** 259 (1981).
49. C. Thomsen, M. Cardona, W. Kress, R. Liu, L. Genzel, M. Bauer, E. Schönherr, and U. Schröder, Solid State Commun. **65,** 1139 (1988).
50. T. Timusk, D. A. Bonn, J. E. Breedan, C. V. Stager, J. D. Garrett, A. H. O'Reilly, and M. Reedyk, in *Proceedings of the International Conference on High Temperature Superconductors and Materials and Mechanisms of Superconductivity* (North-Holland, Amsterdam, 1988), p. 1744.